HHS Public Access

Author manuscript

*Sci Transl Med*. Author manuscript; available in PMC 2022 September 22.

Published in final edited form as:

*Sci Transl Med*. 2021 September 22; 13(612): eabf8629. doi:10.1126/scitranslmed.abf8629.

# MXene-infused bioelectronic interfaces for multiscale electrophysiology and stimulation

**Nicolette Driscoll**[1,2,3], **Brian Erickson**[4], **Brendan B. Murphy**[1,2,3], **Andrew G. Richardson**[2,5], **Gregory Robbins**[6], **Nicholas V. Apollo**[1,2,3], **Georgios Mentzelopoulos**[1,2,3], **Tyler Mathis**[7,8], **Kanit Hantanasirisakul**[7,8], **Puneet Bagga**[9,10], **Sarah E. Gullbrand**[11,12], **Matthew Sergison**[3,5], **Ravinder Reddy**[9], **John A. Wolf**[3,5], **H. Isaac Chen**[3,5], **Timothy H. Lucas**[2,5], **Timothy Dillingham**[6], **Kathryn A. Davis**[2,13], **Yury Gogotsi**[7,8], **John D. Medaglia**[4,13,14], **Flavia Vitale**[1,2,3,6,13,*]

[1]Department of Bioengineering, University of Pennsylvania, Philadelphia, PA 19104, USA

[2]Center for Neuroengineering and Therapeutics, University of Pennsylvania, Philadelphia, PA 19104, USA

[3]Center for Neurotrauma, Neurodegeneration, and Restoration, Corporal Michael J. Crescenz Veterans Affairs Medical Center, Philadelphia, PA 19104, USA

[4]Department of Psychology, Drexel University, Philadelphia, PA 19104, USA

[5]Department of Neurosurgery, University of Pennsylvania, Philadelphia, PA 19104, USA

[6]Department of Physical Medicine and Rehabilitation, University of Pennsylvania, PA 19104, USA

[7]Department of Materials Science and Engineering, Drexel University, Philadelphia, PA 19104, USA

[8]A.J. Drexel Nanomaterials Institute, Drexel University, Philadelphia, PA 19104, USA

[9]Department of Radiology, Center for Magnetic Resonance and Optical Imaging, University of Pennsylvania, Philadelphia, PA 19104, USA

[10]Diagnostic Imaging, St Jude Children's Research Hospital, Memphis, TN 38105, USA

[*]Corresponding author. vitalef@pennmedicine.upenn.edu.

**Author contributions**: N.D. and F.V. designed the study. N.D. and N.V.A. conceptualized the MXtrode devices. N.D. developed the fabrication process, produced all MXtrode devices, performed electrical and electrochemical characterization, captured optical microscopy images, and analyzed all of the electrophysiology data. N.D., B.E., B.B.M., conducted the EEG experiments and analyzed the data with F.V., J.D.M., G.M., and K.A.D. N.D., B.B.M., and G.R. performed EMG, ECG, and EOG experiments and analyzed the data with T.D. and F.V. A.G.R. performed the rat surgery and together with N.D. and T.H.L. performed the cortical stimulation experiment. H.I.C. performed the swine surgery and together with M.S., J.A.W. and N.D. collected the ECoG data. T.M. collected SEM images and K.H. measured the magnetic properties of $Ti_3C_2$ MXene under guidance from Y.G. R.R. advised on and designed MRI experiments and P.B. collected the 9.4T MRI images. S.E.G. collected the CT images. N.D. and F.V. wrote the manuscript with contributions from all authors.

**Competing interests**: F.V., N.D., N.V.A., and Y.G. are co-inventors on international patent application No. PCT/US2018/051084, "Implantable devices using 2D metal carbides and nitrides (MXenes)." F.V., N.D., and N.V.A. are co-inventors on U.S. provisional patent application No. PCT/US2018/051084, "Rapid manufacturing of absorbent substrates for soft, conformable sensors and conductors." B.E. and J.D.M. have served in a consulting and advisory role with Starfish Neuroscience. The remaining authors declare no competing interests.

**Data and materials availability:** All data associated with this study are present in the paper or in the Supplementary Materials. Data sets are publicly available on: https://doi.org/10.6084/m9.figshare.15036012. All code used to generate the results in this work are publicly available on: https://zenodo.org/badge/latestdoi/388516935. $Ti_3C_2$ MXene was obtained via a material transfer agreement between the University of Pennsylvania and MuRata Manufacturing Co. Ltd.

[11]Translational Musculoskeletal Research Center, Corporal Michael J. Crescenz VA Medical Center, Philadelphia, PA 19104, USA

[12]McKay Orthopaedic Research Laboratory, Department of Orthopaedic Surgery, University of Pennsylvania, Philadelphia, PA 19104, USA

[13]Department of Neurology, University of Pennsylvania, Philadelphia, PA 19104, USA

[14]Department of Neurology, Drexel University, Philadelphia, PA 19104, USA

## Abstract

Soft bioelectronic interfaces for mapping and modulating excitable networks at high resolution and at large scale can enable paradigm-shifting diagnostics, monitoring, and treatment strategies. Yet, current technologies largely rely on materials and fabrication schemes that are expensive, do not scale, and critically limit the maximum attainable resolution and coverage. Solution processing is a cost-effective manufacturing alternative, but biocompatible conductive inks matching the performance of conventional metals are lacking. Here, we introduce MXtrodes, a class of soft, high-resolution, large-scale bioelectronic interfaces enabled by $Ti_3C_2$ MXene (a two-dimensional transition metal carbide nanomaterial) and scalable solution processing. We show that the electrochemical properties of MXtrodes exceed those of conventional materials, and do not require conductive gels when used in epidermal electronics. Furthermore, we validate MXtrodes in applications ranging from mapping large scale neuromuscular networks in humans to cortical neural recording and microstimulation in swine and rodent models. Finally, we demonstrate that MXtrodes are compatible with standard clinical neuroimaging modalities.

## One Sentence Summary:

$Ti_3C_2$ MXene-based bioelectronics produced through a highly scalable process enable multiscale electrophysiology and stimulation.

## Introduction

Recent advances in soft materials and electronics have fueled a new generation of bioelectronic technologies for medical diagnostics and therapeutics, healthcare monitoring, and wearable devices (1–4). Soft and flexible bioelectronic devices designed to safely and intimately interface with tissues throughout the human body offer paradigm-shifting opportunities for monitoring brain activity, cardiac health, and muscle function, as well as for facilitating human-machine interactions, such as myoelectric control of advanced prostheses (5–7) or brain-computer interfaces (8). Active bioelectronic devices can also implement intelligent control strategies based on electrical stimulation of excitable circuits for treating neurological diseases (9, 10), heart arrhythmias (11, 12), and inflammatory disorders (13, 14), as well as for rehabilitation therapies (15–17).

Despite considerable progress in the field of soft, ultra-thin, and conformable bioelectronics (18–22), conventional materials and fabrication processes remain largely inadequate for producing large-scale, high-density multielectrode arrays that can map and modulate activity with high spatiotemporal resolution over broad areas in excitable tissues. For example,

thin-film processing has enabled advances in ultra-thin and flexible electronics; however, such processes rely on wafer-scale microfabrication conducted in a cleanroom facility, which is time consuming, expensive, and typically limits the maximum attainable area coverage to a few square centimeters (1). Recent work has demonstrated the possibility to expand this size limit by implementing the fabrication process on large-diameter wafers (19), but microfabrication techniques remain difficult to scale and are not cost-effective. Contributing to manufacturing challenges is the fact that flexible polymeric encapsulation materials require low-temperature processing below their glass transition points and can be incompatible with certain chemicals and solvents commonly used in microfabrication. In addition to the processing constraints, conventional bioelectronic materials – such as gold (Au), platinum (Pt), iridium (Ir), and silver/silver-chloride (Ag/AgCl) – are both costly and intrinsically limited in their electronic, mechanical, and chemical compatibility with biological tissues. For example, they present challenges in achieving low electrode-tissue interface impedance, which is essential for high-fidelity recording and for safe, effective delivery of electrical stimulation. As a result, in applications such as epidermal electronics, conventional Ag/AgCl electrodes typically require a conductive gel at the skin interface to sufficiently lower the impedance to acquire good quality signal. The conductive gels pose issues including skin irritation and impedance instability as they dry out (23, 24). Metal-based devices are also inadequate for coupling with clinical imaging modalities such as magnetic resonance imaging (MRI), often causing artifacts in the images even if they are considered MR safe. To realize the next generation of soft, large-scale, high-density bioelectronic interfaces for human applications, innovation in both materials and fabrication is needed.

Solution processing techniques, such as inkjet or screen printing, offer a scalable and low-cost route for fabricating large-area multielectrode arrays unencumbered by the size constraints of wafer-level methods. Despite these advantages, widespread adoption of such techniques has so far been limited by the lack of conductive inks that can produce electrodes with biocompatibility, flexibility, electronic conductivity, and electrochemical properties comparable to those made with conventional materials. High conductivity can be achieved by printing ink formulations based on metal nanoparticles, however, they typically require high annealing temperatures which are not compatible with soft polymeric substrates (25, 26). Furthermore, metal inks raise concerns about potential toxicity (27). Conducting polymer-based inks, notably those using poly(3,4-ethylenedioxythiophene) (PEDOT) with various dopants such as polystyrene sulfonate (PSS), can be processed at ambient temperatures to generate flexible, biocompatible films, but their conductivity is generally much lower than metal films (28, 29). This has constrained their use predominantly to electrode coatings in devices that require metal interconnects. Furthermore, PEDOT is prone to hydrolysis in wet environments leading to loss of conductivity over time (30). Finally, graphene oxide (GO) inks require an additional reduction step to be converted to the conductive reduced graphene oxide (rGO) form, which poses materials and safety issues due to the high temperatures and toxic chemicals employed in the reduction process (31). Furthermore, the conductivity of rGO is still far inferior to that of pristine graphene (32) and PEDOT:PSS films.

Transition metal carbides, nitrides, and carbonitrides (MXenes) have emerged as a new class of two-dimensional (2D) nanomaterials that enable low-cost, additive-free, solution processing and can produce biocompatible films with metallic conductivity. MXenes are 2D flakes ~1 nm in thickness and up to 10s of μm in lateral size which contain abundant surface-terminating functional groups, including hydroxyl (-OH), oxygen (-O), or fluorine (-F), which make them hydrophilic and also allow for versatile surface modification and functionalization. The unique hydrophilic nature of MXenes enables a wide range of safe, high-throughput, and scalable processing methods using simple water-based inks, including spray (33), spin (34), and dip coating (35), direct writing (36), and inkjet printing (36, 37). Of the large variety of MXenes that have been synthesized to date, $Ti_3C_2$ (the chemical formula is often written as $Ti_3C_2T_x$ to account for the surface terminations, $T_x$) has been the most widely studied and optimized MXene. It is made of Earth-abundant elements and no cytotoxicity has been observed in previous studies (38). Recently, $Ti_3C_2$ has attracted attention for a number of biomedical applications (39), including cancer theranostics (40), hemodialysis (41), and wearable mechanical sensors (42, 43). Our group has pioneered the use of $Ti_3C_2$ for implantable neural microelectrodes (44, 45) and skin-conformable, thin-film wearable sensors (46). $Ti_3C_2$ has metallic behavior exhibiting electronic conductivity of up to 15,000 –20,000 S/cm, higher than all other solution-processed 2D materials (47, 48). Additionally, MXenes are produced using a top-down selective etching procedure which is highly scalable compared to the bottom-up techniques such as physical and chemical vapor deposition required to synthesize many other nanomaterials (49).

In this work, we developed a class of flexible, multichannel, high-density bioelectronic interfaces – which we have named “MXtrodes” – that are capable of both high-fidelity recording and effective stimulation of neural and neuromuscular circuits at multiple scales. We leveraged the excellent processability of $Ti_3C_2$ MXene to develop a rapid, low-cost, and highly scalable method for fabricating multichannel electrode arrays of arbitrary size and geometry. We report a comprehensive study of the electrochemical properties of $Ti_3C_2$ relevant for recording and stimulation of bioelectric circuits, and we demonstrate the utility of MXtrodes for mapping and modulating excitable networks at scales ranging from large neural and muscular circuits in humans to small animal models. We show that gel-free MXtrode arrays for human epidermal recording have electrode-skin interface impedance and recording quality comparable to larger, commercially available pre-gelled Ag/AgCl electrodes. Furthermore, we demonstrate the ability of MXtrodes to map neural and neuromuscular activation patterns at high spatial and temporal resolution and to deliver effective electrical stimulation. Finally, we show that MXtrodes minimally interact with magnetic fields and x-rays, resulting in artifact-free high-field MRI and computed tomography (CT) imaging. The unique properties of $Ti_3C_2$ and the high-throughput, scalable, and cost-effective fabrication process developed here support use of MXtrodes for applications in healthcare, research, and wearable electronics.

## Results

### Rapid, low-cost manufacturing of MXtrodes

We developed a simple method for producing the MXtrode arrays involving: i) laser-patterning a porous absorbent substrate; ii) infusing it with a water-based $Ti_3C_2$ MXene ink; and iii) encapsulating the resulting conductive composite in flexible elastomeric films. We fabricated two types of electrodes to address application-specific requirements by varying the same basic process (Fig. 1A): flat or planar electrodes for epidermal sensing and for cortical brain recording and stimulation, and three-dimensional (3D) “mini-pillar” electrodes for gel-free electroencephalography (EEG).

We used a carbon dioxide ($CO_2$) laser to pattern a nonwoven, hydroentangled cellulose-polyester (60%−40%) blend substrate into the desired electrode array geometry. This served as a scaffold for the MXene flakes, with the laser patterning process allowing for rapid prototyping and customization of the array geometry with feature sizes down to 250 μm, the resolution limit of the laser (fig. S1A). Next, we infused the cellulose-polyester substrate with MXene ink, which was prepared by a minimally intensive layer delamination (MILD) method (50) to produce a water-based MXene ink with a concentration of 20 mg/mL. The ink quickly wicked into the absorbent substrate, coating all the fibers. In principle any absorbent fabric or paper material could be used as the substrate in this process, however the fiber type and alignment can affect the electrical properties. MXene is known to adhere well to natural, negatively charged fibers such as cellulose and cotton (51). We evaluated nonwoven, hydroentangled substrates of several different materials and chose a 60%−40% cellulose-polyester blend as the substrate because after infusing with MXene it showed the highest conductivity and best durability when subjected to cycles of bending (fig. S1, B to E). We also optimized the concentration of MXene ink, finding that a concentration of 20 mg/mL maximized the conductivity and uniformity of the resulting structures. Concentrations higher than 20 mg/mL did not absorb effectively into the substrates due to their high viscosity, instead forming a thick, brittle layer of MXene in the surface layers of the substrate, and concentrations below 0.5 mg/mL did not form a continuous conductive network (fig. S1 F,G).

The MXene-infused substrates were thoroughly dried in a vacuum oven for 1 h. The resulting structure was a rough, macro-porous conductive composite, with MXene flakes coating the individual fibers in the textile matrix. The presence of $Ti_3C_2$ MXene in the resulting composite was confirmed through X-ray diffraction (XRD) and Raman spectroscopy (fig. S2) as well as optical and scanning electron microscopy (SEM) imaging (fig. S3, A,B). For the planar MXtrode arrays, the MXene conductive composite was encapsulated in ~1 mm-thick layers of polydimethylsiloxane (PDMS), with a thorough degassing step prior to curing that allowed the PDMS to infiltrate into the conductive matrix (fig. S3C). In the planar MXtrode arrays for cortical recording and stimulation, an additional 1 μm-thick layer of parylene-C was deposited to serve as an additional barrier to moisture. Electrode contacts were defined by cutting through the top encapsulation layer with a biopsy punch of the desired electrode diameter and removing the polymer disk to expose the conductive MXene composite beneath (fig. S3D). To fabricate 3D MXtrode arrays for

gel-free EEG recording, “mini-pillars” of MXene-infused cellulose foam 3 mm in height were deposited onto the electrode locations prior to PDMS encapsulation. Similar to the absorbent cellulose-polyester substrate, the cellulose foam readily absorbed the MXene ink, which thoroughly coated all surfaces to form a porous conductive composite after vacuum drying (fig. S3E). No adhesive was required to affix the 3D mini-pillars to the underlying laser-patterned substrate: inking the two structures with MXene and vacuum drying them while in contact resulted in the formation of a continuous conductive network fusing the laser-patterned substrate and the cellulose foam together, which was further reinforced after polymer encapsulation. Mechanical testing confirmed the durability of the connection between the mini-pillar and underlying substrate (fig. S4). 3D MXtrode array fabrication was completed by PDMS encapsulation and trimming of the mini-pillars to expose the conductive MXene-cellulose foam composite. The versatility, simplicity, scalability, and low cost of this process enabled parallel fabrication of MXtrodes in different geometries within the same batch for diverse bioelectronic applications (Fig. 1, B to E, fig. S5).

## Electrical and electrochemical properties of MXtrodes

In the MXtrode arrays, the MXene-cellulose-polyester conductive composite forms the wires which carry the signal out to the recording amplifier. Thus, it is important that this composite is highly conductive to reduce ohmic losses, minimize noise, and acquire high-quality signals. The bulk conductivity of the MXene composites was 3015 ± 333 S/m (fig. S6) which is in agreement with previously reported values for MXene-coated cellulose fibers (51). To highlight the conductivity advantage of $Ti_3C_2$ MXene compared to other conductive inks – which could in principle be used in our fabrication process – we also fabricated conductive composites using PEDOT:PSS and rGO inks with the same cellulose-polyester absorbent substrate. The bulk conductivity of PEDOT:PSS and rGO composites was 7.6 ± 0.4 S/m and 0.005 ± 0.002 S/m, respectively, both lower than that of MXene (fig. S6).

To evaluate the impedance and charge transfer properties of MXene electrodes, we conducted electrochemical measurements in phosphate buffered saline (PBS) on MXtrodes with diameters ranging from 500 μm to 3 mm and compared them to 2 mm-diameter Pt electrodes. Specifically, we performed electrochemical impedance spectroscopy (EIS), cyclic voltammetry (CV) and voltage transient (chronopotentiometry) experiments to measure the impedance magnitude, charge storage capacity (CSC), water window, and charge injection capacity (CIC) of each electrode, and to determine how these properties scaled with electrode diameter. Data are shown in Table 1 and included in Data File S1, and literature values for other common electrode materials are shown in table S1. EIS revealed that the MXtrodes of all diameters tested showed greatly reduced impedance compared to the Pt electrodes at frequencies below 200 Hz – where impedance is dominated by the electrochemical properties of the electrode interface (52) and where most physiologic signals of interest lie (Fig. 2A). At 10 Hz, the impedance of the MXtrodes ranging from 500 μm to 3 mm was 1343.3 ± 81.6 Ω (500 μm), 644.2 ± 97.3 Ω (1 mm), 451.2 ± 35.4 Ω (2 mm), and 241.4 ± 14.7 Ω (3 mm), while the impedance of the Pt electrodes was 8918.3 ± 1147.7 Ω (2 mm). At the reference frequency of 1 kHz – where the interface impedance is controlled by the solution resistance, resistance of wires connecting the electrode, and electrode size (52) – the impedance of size-matched MXtrodes is slightly higher than Pt, likely due to the

higher resistance of MXtrode wires compared to Pt (Fig. 2A, Table 1). We attribute the low impedance of the MXtrodes to the highly porous and rough morphology of the electrodes, which endows the interface with a high effective surface area.

The electrochemical stability window for MXtrodes determined from wide-scan CVs is −1.7 to +0.6 V (fig. S7, A,B), showing that MXene is exceptionally stable in the cathodic region. Water electrolysis was observed beginning at −1.9 V, and −1.7 V was therefore chosen as a conservative cathodic limit. In the anodic region, evidence of faradaic current was observed beginning at +0.7 V, and +0.6 V was therefore chosen as the anodic limit. This wide potential range is advantageous for therapeutic electrical stimulation applications, and while the anodic potential limit (+0.6 V) is slightly lower than that of Pt, platinum-iridium (PtIr), or iridium oxide (IrOx) (+0.8 V), stimulation waveforms can be engineered to minimize voltage excursions in the anodic range while taking advantage of the large cathodic limit (53–55). Whereas previous studies have reported anodic oxidation of $Ti_3C_2$ films at +430 mV (56), we observed no oxidation peak or current loss when MXtrodes were cycled within the range of −1.7 to +0.6 V for up to 50 cycles (fig. S7C). The extended anodic stability limits may result from lower current densities at the electrode surface, as previously reported for other electrodes with a rough surface topology (57).

Analysis of cathodic CSC ($CSC_C$) for MXtrodes and Pt electrodes from CVs at 50 mV/s within their respective water windows revealed enhanced capacitive charging and charge delivery for MXtrodes with ~100 times larger $CSC_C$ than Pt electrodes (Table 1, fig. S7D). To place these results in the broader context of bioelectronic materials, we show $CSC_C$ values for a variety of other common electrode materials in table S1. To enable a more direct comparison of $CSC_C$ values between MXtrodes and Pt electrodes, we also ran CV scans in the intersection of the MXene and Pt voltage windows, –0.6 to +0.6 V (Fig. 2B and fig. S7E). Within this more constrained voltage range, the MXtrodes showed greater than 20 times enhanced $CSC_C$ compared to Pt, which we attribute both to the high intrinsic capacitance of $Ti_3C_2$ MXene (58–60) and to the high effective surface area of the MXtrode surface (table S2). The expected nonlinear relationship between $CSC_C$ and electrode diameter observed for the MXtrodes (fig. S7F) reflects the known phenomenon of electrochemical charge exchange happening predominantly at the edge of the electrode (55, 61).

Next, we measured the voltage transients evolved on each electrode when used to deliver charge-balanced, cathodic-first biphasic current pulses ranging from 1 to 5 mA with a duration of 500 μs in both phases ($t_c$, $t_a$) and an interpulse interval ($t_{ip}$) of 250 μs (Fig. 2C and fig. S7, G to J). For the 500 μm-diameter MXtrodes, the current amplitude range was restricted to 600 μA to 2 mA. The maximum cathodic excursion potential, $E_{mc}$, was taken 10 μs after the cathodic pulse end and $CIC_C$ was defined as the injected charge at which $E_{mc}$ would reach the water reduction potential. The resulting $CIC_C$ values reveal that the MXtrodes outperform Pt electrodes, with MXtrodes showing ~10 times larger $CIC_C$ than the Pt electrodes (Table 1). $CIC_C$ values for several other common electrode materials are shown in table S1, although we note that drawing direct comparisons between electrodes that are not size-matched is problematic due to the nonlinear scaling relations of these properties. MXtrodes show a larger access voltage ($V_a$) compared to Pt, which we attribute to the

ohmic resistance of the MXtrode wire leading to the electrode. Still, the enhanced $CIC_C$, has implications for stimulation applications and suggests that MXtrodes could offer more efficient charge transfer than current state-of-the-art Pt electrodes. The scaling dependency of $CIC_C$ on electrode diameter for the MXtrodes (fig. S7K) revealed the expected nonlinear scaling dependency resulting from edge effects. A schematic depicting the relative sizes of the MXtrodes included in the analysis is shown in fig. S7L.

Finally, we evaluated the impedance of MXtrodes at the interface with human skin. Achieving low electrode-skin impedance is key for recording high-fidelity signals (62, 63) and becomes particularly challenging in gel-free structures like MXtrodes. Thus, we measured EIS for 3 mm-diameter MXtrodes, both in planar and 3D configurations, on clean human skin following standard preparation with an alcohol swab and light abrasion. At 1 kHz, the planar and 3D MXtrodes showed impedances of 6.6 ± 2.9 kΩ and 4.9 ± 2.6 kΩ, respectively, with the lower impedance of the 3D electrodes attributable to the improved contact from the mini-pillars pressing into the skin (Fig. 2D). When normalized by their geometric surface area (GSA) of 0.071 $cm^2$, the impedance is 0.47 ± 0.20 kΩ·$cm^2$ for planar and 0.35 ± 0.12 kΩ·$cm^2$ for 3D MXtrodes, which are among the best values reported for dry, gel-free epidermal electrodes (1, 64, 65) and ~100 times lower than those of commercially available gelled Ag/AgCl electrodes commonly used for electrodiagnostics and monitoring (46).

## Epidermal sensing in humans

We investigated gel-free MXtrodes for human epidermal sensing applications, using custom geometries designed for each application. First, we acquired scalp EEG on a healthy human subject using 3D MXtrodes and standard gelled Ag/AgCl EEG electrodes for comparison. We designed an 8-channel (ch) MXtrode array, with 3 mm-diameter mini-pillar electrodes arranged in a ring around a central opening, where we placed a standard 1 cm-diameter gelled Ag/AgCl EEG electrode for side-by-side comparison of simultaneously acquired EEG (Fig. 3A). In the first EEG task, we placed the MXtrode array over the parietal region near EEG site P1 (as defined in the EEG 10–20 system, located over inferior parietal cortex to the immediate left of the midline) (Fig. 3B). Ground and reference for all EEG recordings were gelled Ag/AgCl electrodes placed at the center forehead and left mastoid, respectively. Before placing the electrodes on the skin, the entire recording area was cleaned with an alcohol swab and lightly abraded. The electrode-skin interface impedance at 1 kHz for the dry MXtrodes was 2.8 ± 0.9 kΩ, while the impedance of the larger gelled Ag/AgCl electrode during the same experiment was 1.2 kΩ at 1 kHz (Fig. 3C). Given the critical role of the electrode-skin interface impedance in determining the quality of scalp EEG signals (66), the low impedance of mm-scale, gel-free MXtrodes is notable and enables high-resolution EEG recording with dense arrays. We recorded EEG in 2 min sessions, with the subject alternating eyes open and eyes closed resting states. In both states, the EEG signal recorded on the dry MXtrodes was comparable to the signal recorded on the gelled Ag/AgCl electrode (Fig. 3D). A clear 10 Hz alpha rhythm emerged in the eyes closed state with a higher amplitude than in the eyes open condition (Fig. 3, E,F). This alpha signature is one of the most reliable and widely studied behaviorally-linked EEG signatures in human subjects research (67). During the recording session, there was no

significant difference between the mean alpha bandpower across the electrodes ($P > 0.05$, one-way ANOVA), confirming that the signals were comparable between the dry MXtrodes and the gelled Ag/AgCl electrode (fig. S8). Interestingly, however, when alpha bandpower values were calculated in 1 s windows with 0.5 s of overlap and observed sequentially, distinct spatiotemporal patterns of alpha activation emerged even across the small scalp area sampled (movie S1).

For the second EEG task, the electrodes were removed and replaced over the hand motor area which was localized using single pulses of transcranial magnetic stimulation (TMS) to evoke lateral finger movements (fig. S9A). The subject performed 2 min periods of imagined and actual hand flexion while EEG was recorded simultaneously with the co-located MXtrodes and gelled Ag/AgCl electrode. During this motor task, we also found that the EEG signal was comparable between the two electrode types. Furthermore, we observed a suppression of the 8–12 Hz motor mu rhythm during the actual hand flexion relative to the imagined hand flexion (fig. S9B). The mu suppression signature during imagined hand movement is an important EEG feature which has been successfully used as a control signal for EEG-based brain-computer interfaces (BCIs) (68, 69).

Following these experiments, we performed EEG recording on N=3 additional subjects using a different montage to further highlight the advantages of mm-scale gel-free MXtrodes for high-density EEG mapping. In these experiments, two 16-ch arrays of 3 mm-diameter 3D mini-pillar MXtrodes arranged in a 4×4 grid with 3 mm inter-electrode spacing were placed over the F3 and F4 EEG 10–20 positions. This yielded 32-ch bi-frontal recordings, with density exceeding the densest configurations of traditional Ag/AgCl electrodes in common use today (the 10–5 system). We mapped alpha bandpower activation during eyes closed resting states, and found distinct spatiotemporal activation patterns across the arrays, which was consistent across subjects (fig. S10 and movie S2). These findings support recent evidence that the “spatial Nyquist rate”, or inter-electrode distance sufficient to extract the maximum possible resolution from scalp EEG signals, is smaller than previous estimates which posited that 20–30 mm electrode spacing is sufficient (70). Together, the results of these EEG experiments confirmed that mm-scale, gel-free MXtrodes can record EEG signal at least as well as standard gelled Ag/AgCl EEG electrodes, while also improving spatiotemporal resolution for high-density EEG applications.

Next, we evaluated MXtrodes for high-density surface electromyography (HDsEMG) recording to map muscle activation and localize innervation zones (IZs). HDsEMG recordings require flexible, large-area, and high-density electrode arrays capable of covering the wide range of muscle sizes. We created custom MXtrode HDsEMG arrays to map muscle activation and localize IZs in two muscle groups of different sizes (Fig. 4). First, we used a 20-ch planar MXtrode array placed over the *abductor pollicis brevis* (APB) at the base of the thumb. In this experiment, the 3 mm-diameter dry MXtrodes had an average electrode-skin interface impedance of 54.6 ± 28.4 kΩ at 1 kHz (fig. S11A). We stimulated the median nerve to evoke APB contractions and recorded the EMG on the MXtrode array. We calculated the mean evoked muscle response across stimulation trials (Fig. 4A) and constructed a latency map of the peak of the evoked response. The location with the shortest

latency indicates the location of the IZ, which can be seen overlaid on the subject's hand in Fig. 4B, and it is in good agreement with expectations based on anatomical landmarks (71).

Following the APB mapping experiment, we mapped the activation of the larger *biceps brachii* with a 40-ch planar MXtrode array. Here, the 3 mm-diameter dry MXtrodes had an average electrode-skin interface impedance of 22.0 ± 14.3 kΩ at 1 kHz (fig. S11B). Unlike the smaller APB muscle, which has a small and spatially confined IZ corresponding to a single neuromuscular junction (NMJ), the larger *biceps brachii* has distributed NMJs in IZ regions that run perpendicular to the muscle (72). We used two different methods to localize these IZs in the biceps: first we stimulated the supraclavicular nerve and constructed a latency map of the peak evoked response, similar to the methods used for the APB (Fig. 4, C,D). This produced a clear mapping of the IZ location as the region with the shortest latency, running across the short head of the *biceps brachii*. Second, we recorded motor unit action potentials (MUAPs) as the subject performed isometric contractions of the biceps (fig. S11 C,D). In these recordings, bipolar subtraction of the raw EMG signal along the length of the biceps muscle revealed MUAPs that propagated outward in both directions from the IZ, with signal inversion and a clear latency as the MUAP traveled away from the IZ (fig. S11D). Localization of the biceps IZ obtained from both methods were in excellent agreement with each other, and with previous reports (72). These results demonstrate that dry, high-resolution MXtrode arrays are capable of mapping muscle activation with high accuracy to precisely localize IZs in both small and large muscle groups.

In addition to the HDsEMG mapping experiments, we also evaluated the susceptibility of dry MXtrodes to motion and pressure-induced artifacts. To test motion artifacts, we recorded EMG from the forearm using 3 mm-diameter planar MXtrodes placed adjacent to a 20 mm-diameter gelled Ag/AgCl control electrode. The subject alternated between a stationary pinch grip to produce EMG, and a relaxed grip while raising and lowering the forearm using the opposite hand to minimize muscle activation (fig. S12A). Motion introduced small deflections in the signal which were low in amplitude and frequency could be easily removed by a standard EMG bandpass filter (fig. S12 B,C). Notably, the artifacts were larger in amplitude on the gelled electrode compared to the MXtrodes. Next, we evaluated pressure-induced artifacts, which are relevant in applications such as EMG-controlled prosthetics, where electrodes located in a prosthetic socket can experience substantial normal forces. Similar to the motion artifacts, we observed small deflections recorded on the MXtrodes during changes in pressure, which could also be easily filtered out with a standard bandpass filter (fig. S13).

Next, we acquired electrocardiogram (ECG) recordings on a healthy human subject with 1.3 cm-diameter MXtrodes in a simplified 3-electrode montage (Fig. 5A). We recorded sequentially from MXtrodes and from 2 cm-diameter pre-gelled Ag/AgCl electrodes, placed in the same locations. The dry MXtrodes and pre-gelled electrodes had average 1 kHz skin-electrode impedances of 1.29 kΩ and 1.38 kΩ, respectively. On both types of electrodes, characteristic ECG features were clearly visible, with the P wave followed by the QRS complex and the T wave (Fig. 5, B,C). These results confirmed that dry MXtrodes can record the ECG with signal quality comparable to standard clinical gelled electrodes.

As a final demonstration of MXtrodes for human epidermal sensing, we acquired electrooculography (EOG), which has applications in ophthalmological diagnosis, BCIs, and for monitoring attention and fatigue (73, 74). The EOG signal arises from the standing dipole potential between the positively charged cornea and the negatively charged retina, which enables tracking eye movements as this dipole is rotated. With the same 1.3 cm-diameter dry MXtrode geometry used in ECGs, we recorded the EOG in two configurations to track up-down and left-right eye movements. By placing MXtrodes above and below the eye, recorded voltage fluctuations could be decoded to track the up and down movements of the eye (fig. S14, A,B). Similarly, placing MXtrodes on both sides of the eyes enabled decoding the left-right movements (fig. S14, C,D).

## Cortical neural recording and microstimulation with MXtrodes

We next sought to evaluate MXtrodes for implantable sensing and stimulation applications, given their favorable electrochemical properties. One such application is intraoperative electrocorticography (ECoG), a common mapping technique used in resective brain surgery for epilepsy or tumors. We acquired ECoG recordings in an anesthetized swine, a relevant model system in neuroscience given its gyrencephalic structure and neuro-anatomical similarity to the human brain. In this experiment we inserted a 6-ch array of 500 μm-diameter planar MXtrodes through an 8 mm craniotomy/durotomy and placed MXtrodes in direct contact with the cortical surface (Fig. 6A). The array configuration consisted of 3 rows of electrode pairs with 5 mm inter-row spacing and 4.5 mm pitch, so that the rows of electrodes spanned several cortical gyri. A few seconds of representative raw ECoG signal are shown in Fig. 6B. The signals were large in amplitude with negligible 60 Hz noise interference, as evidenced by the power spectra (Fig. 6C). Furthermore, maps of interpolated voltage across the MXtrode array revealed stereotyped spatial patterns emerging during the “up” and “down” states in the ECoG signal (Fig. 6 D,E), highlighting the utility of cortical brain mapping with MXtrodes.

In addition to ECoG recording, direct stimulation of the cortical surface is used clinically for intraoperative cortical mapping (75) and neuromodulation therapies (76), as well as for closed-loop BCIs (77). Given that the MXtrodes showed superior CSC and CIC compared to Pt, a material commonly used in stimulating electrodes, we sought to demonstrate the effectiveness of MXtrodes for electrical stimulation by evoking motor responses via intraoperative stimulation in rat brain. We placed a 500 μm-diameter planar MXtrode subdurally onto the whisker motor cortex of an anesthetized rat. Contralateral to the MXtrode, an optical micrometer was positioned to track whisker displacement, with one whisker placed into a plastic tube to maximize detection sensitivity (Fig. 6F). Trains of charge-balanced, cathodic-first stimulation pulses with 300 μs half-phase period and amplitudes ranging from 1.0 to 1.4 mA were delivered through the MXtrode. We observed stimulation-evoked whisker movements for amplitudes greater than 1.0 mA, with the whisker deflection amplitude scaling with the stimulation intensity (Fig. 6, G to I and movie S3). Whisker movements registered as oscillatory deflections on the micrometer, with the first deflection peak always being the largest in amplitude. To compare whisker deflection across stimulation current amplitudes, we computed the mean amplitude of the first whisker

deflection across stimulation trials at each current amplitude. These results confirm that MXtrodes can deliver electrical stimulation to effectively modulate neural activity.

Finally, we evaluated the stability of MXtrodes to stimulation pulses by subjecting 500 μm-diameter MXtrodes to 1000 cycles of 1.2 mA biphasic stimulation in PBS, with stimulation parameters matching those shown to evoke whisker movements in vivo (i.e. charge-balanced, cathodic-first pulses with 300 μs half-phase period). This corresponds to a cathodic charge density of 0.18 mC/cm$^2$, which is within the range of the charge injection limit. Impedance spectra for the MXtrodes measured before and after repeated pulsing showed no change in the impedance behavior, indicating good stability to repeated cycles of stimulation (fig. S15).

## Compatibility of MXtrodes with clinical imaging

With the widespread adoption of bioelectronic technologies, compatibility with clinical imaging has become increasingly important. MRI and CT are the two most common imaging techniques used in the diagnosis of injury and disease, as well as in image-guided interventions. In the MRI environment, mismatch in magnetic susceptibility between the device materials and the tissue produces imaging artifacts that shadow the surrounding anatomical structures (78), a challenge that is compounded at high field strengths which are increasingly being used for high resolution imaging (79). Although the magnetic susceptibility of $Ti_3C_2$ MXene had not been previously characterized, we hypothesized from the weak dia- and paramagnetic properties of C and Ti, respectively, that $Ti_3C_2$ may have a low magnetic susceptibility and thus prove compatible with the MR environment. To verify our hypotheses, we performed MRI scans of MXtrodes and measured the magnetic properties of $Ti_3C_2$ at body temperature. We imaged cross-sections of 3 mm-diameter planar MXtrodes and 2.3 mm-diameter commercial Pt electrodes embedded in conductive agarose phantoms in a 9.4T high-field research MRI system (Fig. 7A). In the MR images, we found substantial shadowing around the Pt electrodes, while no artifact was visible around the MXtrode (Fig. 7B). The MXene composite forming the conductive electrode was almost completely indistinguishable from the surrounding PDMS encapsulation. To further explore the MRI compatibility of the MXtrodes, we next imaged an array of 3 mm-diameter 3D mini-pillar MXtrodes in a 3T clinical MRI scanner. The MXtrodes were placed atop a tissue phantom and imaged using a battery of scan sequences typical of structural and functional MRI (fMRI). Regardless of the scan sequence, the MXtrodes showed no artifact and were nearly invisible in the images (fig. S16A). Thermal infrared (IR) images and continuous temperature monitoring of the MXtrode array during the phantom scanning showed no evidence of heating (fig. S16 B,C). Following these safety evaluations, we conducted the same battery of structural and functional scan sequences on a human subject with the device placed on the forehead. As before, no artifacts or image distortions were observed around the MXtrode array (Fig. 7 C to E).

To support these findings, we measured the magnetic susceptibility of a $Ti_3C_2$ free-standing film at 310 K, and found it to be 0.21 ppm (fig. S16D), indicating that $Ti_3C_2$ is weakly paramagnetic with magnetic susceptibility very close to that of human tissues (−11.0 to −7.0 ppm). This innate property of $Ti_3C_2$ leads directly to the excellent compatibility of the

MXtrodes with MRI. For comparison, the magnetic susceptibility of Pt is 279 ppm, more than an order of magnitude larger than the susceptibility of human tissues (78). In situations where it might be important for implanted electrodes to be visible in MRI images, such as in epilepsy seizure foci localization relative to electrode locations, a marker such as iron oxide nanoparticles could in principle be incorporated into the electrode contacts to aid in their visualization (80).

In CT imaging, X-ray attenuation resulting from the high density and large atomic mass of metals in conventional electrodes poses challenges (81). Multilayer $Ti_3C_2$ MXene has a density of about 4 g/cm$^3$, which is ~5 times lower than Pt. Thus, we hypothesized that $Ti_3C_2$ could minimize attenuation and scattering artifacts in CT. To test our hypothesis, we imaged 3 mm-diameter planar MXtrodes and 2.3 mm-diameter commercial Pt electrodes embedded in conductive agarose phantoms in a microCT scanner. As expected from the density matching considerations, we observed X-ray scattering artifacts around the Pt electrodes, but not around the MXtrodes (Fig. 7F).

## Discussion

In this work we developed a class of MXene-based bioelectronic interfaces and demonstrated their use for high-fidelity recording and effective stimulation of neural and neuromuscular circuits across multiple scales. The simple fabrication method reported here offers a scalable and low-cost means of producing large-area, multichannel electrode arrays from high performance, solution processable 2D materials. The method is conducive to large-scale manufacturing, a key aspect for translation beyond the lab and into clinical and consumer markets. It also enables rapid customization of array geometries for various applications as well as for patient- or subject-specific fit where desired. These advantages separate this work from previously described thin-film tattoo-like arrays (5, 20), which require time consuming, complex, and costly microfabrication, as well as photomasks to define geometries.

$Ti_3C_2$ endows MXtrodes with low impedance and excellent charge delivery properties, which were evaluated for a range of electrode sizes. In epidermal sensing applications, the low interface impedance of gel-free MXtrodes opens possibilities for high-resolution EMG and EEG, while eliminating the challenges associated with conductive gels. Compared to other recent works demonstrating gel-free epidermal electrodes with Ag-Au core-shell nanowires (82) and commercially available carbon conductive inks (83), our electrodes show greatly reduced electrode-skin interface impedance. In addition to their low interface impedance, the high CSC and CIC of MXtrodes suggest that they may represent a suitable alternative for stimulation electrodes with enhanced charge transfer efficiency and reduced power consumption, although further evaluation of the chronic in vivo safety and stability during stimulation is needed.

In HDsEMG mapping, MXtrode arrays hold promise for applications in neuromuscular diagnostics and rehabilitation, such as for localization of NMJs to target chemodenervation therapies for muscle spasticity and excessive muscle tone. In the future, this may eliminate the need for invasive intramuscular needle EMG stimulation in search of the NMJ. In

scalp EEG, the dry electrode system enabled by 3D MXtrodes may offer a route toward minimizing skin breakdown and alleviating key challenges associated with current gelled systems, such as the time required to apply each electrode and impedance fluctuations over time as the gels dry out. These advantages, coupled with the possibility for obtaining high density EEG recording with mm-scaled MXtrodes, also make this technology attractive for neuroscience research, non-invasive BCI systems, neuro-rehabilitation, and brain-controlled videogaming. Finally, the compatibility of MXtrodes with both MRI and CT imaging enables accurate, artifact-free imaging. This opens exciting possibilities for multimodal studies in both clinical diagnostics and neuroscience research, such as those combining simultaneous EEG with functional MRI or GluCEST imaging (84, 85).

Several limitations of this study should be noted. The voltage limits that define the water window of MXtrodes cannot be equated to the voltage limits for “safe stimulation” without further in vivo testing and histological evaluation, as tissue damage from stimulation is influenced by many factors, including pulse frequency, duty cycle, current density, and electrode size (86). Scalp EEG recordings were limited to subjects with short (i.e. <1 cm long) hair to ensure the 3D mini-pillar electrodes, which were 5 mm in height, could achieve adequate contact with the scalp. In the future, optimization of 3D electrode geometries may enable EEG recording in subjects with longer hair. Additionally, the small area coverage of the EEG electrode montages that we used limited our ability to use independent component analysis (ICA), because interpretation of ICA components is facilitated by visualization of scalp topographies, which are limited in a small array. Finally, in all epidermal recordings, skin preparation including light abrasion was needed to reduce contact impedance and achieve consistent recording quality across subjects, because skin impedance is highly variable between subjects when no skin treatment is used (63).

Overall, our results indicate that MXene-based bioelectronics hold great potential for advanced healthcare diagnostics, monitoring and therapy, as well as for research and consumer electronics. Future directions include evaluating and improving the stability of $Ti_3C_2$ for long-term use (48, 87), optimizing the MXene infusion process to maximize the MXene loading and conductivity of the resulting composite (51), and exploring alternative encapsulation materials to further improve the flexibility and breathability of the electrode arrays (19).

## Materials and Methods

### Study design

The purpose of this study was to develop $Ti_3C_2$ MXene-based bioelectronic devices and to evaluate their properties and performance in recording electrophysiology and delivering electrical stimulation. The epidermal recording performance of MXtrodes was evaluated by performing EEG, EMG, EOG, and ECG recording on healthy human subjects affiliated with the University of Pennsylvania and Drexel University. The EEG recording experiment was approved by the Institutional Review Board (IRB) of Drexel University (Protocol # 1904007140) and the other epidermal recording experiments were approved by the University of Pennsylvania IRB (Protocol # 831802). Informed consent was obtained after the nature and possible consequences of the study was explained. In each epidermal

recording experiment, the recording performance of MXtrodes was compared to clinical standard pre-gelled electrodes for the specific application. The performance of MXtrodes for cortical brain recording and stimulation was evaluated in pigs and rats, respectively. All animal studies were approved by the University of Pennsylvania Institutional Animal Care and Use Committee. For this pilot study, data from N=1 subject or animal was collected for the following applications: EMG, EOG, ECG, ECoG, and cortical stimulation. Data from N=4 subjects was collected for EEG. Experiments were not blinded, there was no randomization, and there were no exclusions of data.

### Statistical analysis

Data are presented with mean values ± SD, unless otherwise noted in the figure caption. One-way analysis of variance (ANOVA) with post-hoc analysis was used for multiple comparisons of mean EEG alpha bandpower among electrodes. Significance was defined as $P < 0.05$. Statistical analysis was performed using MATLAB (R2018a, MathWorks Inc).

## Supplementary Material

Refer to Web version on PubMed Central for supplementary material.

## Acknowledgments:

We thank Prof. Steven J. May (Drexel University) for providing access to the Quantum Design EverCool II physical property measurement system.

**Funding**: This work was supported by: the National Science Foundation Graduate Research Fellowship Program grant no. DGE-1845298 (N.D. and B.B.M.); the National Institutes of Health (NIH) grants no. K12HD073945 (F.V.) and R01NS121219 (F.V. and J.D.M.); the Linda Pechenik Investigator Award, Penn Health Tech Medical Device Accelerator Award, MuRata Manufacturing Co., Ltd., the Mirowski Family Foundation and Neil and Barbara Smit (F.V.); the NIH Office of the Director grant no. DP5-OD021352 (J.M.); the NIH training Fellowship in Neuroengineering and Medicine grant no. T32NS091006 (N.V.A.); the National Institute of Biomedical Imaging and Bioengineering (NIBIB) grant no. P41 EB015893 (R.R.); the Department of Veterans Affairs grant no. IK2 RX003118 (S.E.G.); the Department of Defense (DoD) Epilepsy Research Program (ERP) grant no. W81XWH-16-1-0675 (J.A.W.); exploration of magnetic and electrical properties of MXene was supported by U.S. Department of Energy (DOE), Office of Science, Office of Basic Energy Sciences grant no. DESC0018618 (Y.G.); Any opinions, findings, conclusions, or recommendations expressed in this material are those of the authors and do not necessarily reflect the views of the National Science Foundation.

## References and Notes:

1. Heikenfeld J, Jajack A, Rogers J, Gutruf P, Tian L, Pan T, Li R, Khine M, Kim J, Wang J, Kim J, Wearable sensors: Modalities, challenges, and prospects, Lab Chip 18, 217–248 (2018). [PubMed: 29182185]
2. Rogers JA, Someya T, Huang Y, Materials and mechanics for stretchable electronics, Science (80-. ). 327, 1603–1607 (2010).
3. Liu Y, Pharr M, Salvatore GA, Lab-on-Skin: A Review of Flexible and Stretchable Electronics for Wearable Health Monitoring, ACS Nano 11, 9614–9635 (2017). [PubMed: 28901746]
4. Vitale F, Litt B, Bioelectronics: the promise of leveraging the body's circuitry to treat disease, Bioelectron. Med 1, 3–7 (2018).
5. Norton JJS, Lee DS, Lee JW, Lee W, Kwon O, Won P, Jung SY, Cheng H, Jeong JW, Akce A, Umunna S, Na I, Kwon YH, Wang XQ, Liu ZJ, Paik U, Huang Y, Bretl T, Yeo WH, Rogers JA, Bao Z, Soft, curved electrode systems capable of integration on the auricle as a persistent brain-computer interface, Proc. Natl. Acad. Sci. U. S. A 112, 3920–3925 (2015). [PubMed: 25775550]

6. Jeong JW, Yeo WH, Akhtar A, Norton JJS, Kwack YJ, Li S, Jung SY, Su Y, Lee W, Xia J, Cheng H, Huang Y, Choi WS, Bretl T, Rogers JA, Materials and optimized designs for human-machine interfaces via epidermal electronics, Adv. Mater 25, 6839–6846 (2013). [PubMed: 24327417]
7. Xu B, Akhtar A, Liu Y, Chen H, Yeo WH, Park S, Boyce B, Kim H, Yu J, Lai HY, Jung S, Zhou Y, Kim J, Cho S, Huang Y, Bretl T, Rogers JA, An Epidermal Stimulation and Sensing Platform for Sensorimotor Prosthetic Control, Management of Lower Back Exertion, and Electrical Muscle Activation, Adv. Mater 28, 4462–4471 (2016). [PubMed: 26469201]
8. McFarland DJ, Wolpaw JR, EEG-based brain–computer interfaces, Curr. Opin. Biomed. Eng 4, 194–200 (2017). [PubMed: 29527584]
9. Lee S, Peh WYX, Wang J, Yang F, Ho JS, Thakor NV, Yen SC, Lee C, Toward Bioelectronic Medicine—Neuromodulation of Small Peripheral Nerves Using Flexible Neural Clip, Adv. Sci 4, 1700149 (2017).
10. DeLong MR, Wichmann T, Basal ganglia circuits as targets for neuromodulation in Parkinson diseaseJAMA Neurol. 72, 1354–1360 (2015). [PubMed: 26409114]
11. Irisawa H, Brown HF, Giles W, Cardiac pacemaking in the sinoatrial node Physiol. Rev 73, 197–227 (1993). [PubMed: 8380502]
12. Hwang GT, Park H, Lee JH, Oh S, Il Park K, Byun M, Park H, Ahn G, Jeong CK, No K, Kwon H, Lee SG, Joung B, Lee KJ, Self-powered cardiac pacemaker enabled by flexible single crystalline PMN-PT piezoelectric energy harvester, Adv. Mater 26, 4880–4887 (2014). [PubMed: 24740465]
13. Ulloa L, Quiroz-Gonzalez S, Torres-Rosas R, Nerve Stimulation: Immunomodulation and Control of Inflammation Trends Mol. Med 23, 1103–1120 (2017). [PubMed: 29162418]
14. Cheng J, Shen H, Chowdhury R, Abdi T, Selaru F, Chen JDZ, Potential of Electrical Neuromodulation for Inflammatory Bowel Disease, Inflamm. Bowel Dis 26, 1119–1130 (2020). [PubMed: 31782957]
15. Granat MH, Ferguson ACB, Andrews BJ, Delargy M, The role of functional electrical stimulation in the rehabilitation of patients with incomplete spinal cord injury observed benefits during gait studies, Paraplegia 31, 207–215 (1993). [PubMed: 8493035]
16. Peckham PH, Knutson JS, Functional Electrical Stimulation for Neuromuscular Applications, Annu. Rev. Biomed. Eng 7, 327–360 (2005). [PubMed: 16004574]
17. Ethier C, Oby ER, Bauman MJ, Miller LE, Restoration of grasp following paralysis through brain-controlled stimulation of muscles, Nature 485, 368–371 (2012). [PubMed: 22522928]
18. Nawrocki RA, Jin H, Lee S, Yokota T, Sekino M, Someya T, Self-Adhesive and Ultra-Conformable, Sub-300 nm Dry Thin-Film Electrodes for Surface Monitoring of Biopotentials, Adv. Funct. Mater 28, 1803279 (2018).
19. Tian L, Zimmerman B, Akhtar A, Yu KJ, Moore M, Wu J, Larsen RJ, Lee JW, Li J, Liu Y, Metzger B, Qu S, Guo X, Mathewson KE, Fan JA, Cornman J, Fatina M, Xie Z, Ma Y, Zhang J, Zhang Y, Dolcos F, Fabiani M, Gratton G, Bretl T, Hargrove LJ, Braun PV, Huang Y, Rogers JA, Large-area MRI-compatible epidermal electronic interfaces for prosthetic control and cognitive monitoring, Nat. Biomed. Eng 3, 194–205 (2019). [PubMed: 30948811]
20. Kim DH, Lu N, Ma R, Kim YS, Kim RH, Wang S, Wu J, Won SM, Tao H, Islam A, Yu KJ, Il Kim T, Chowdhury R, Ying M, Xu L, Li M, Chung HJ, Keum H, McCormick M, Liu P, Zhang YW, Omenetto FG, Huang Y, Coleman T, Rogers JA, Epidermal electronics, Science (80-. ). 333, 838–843 (2011).
21. Viventi J, Kim D-H, Vigeland L, Frechette ES, a Blanco J, Kim Y-S, Avrin AE, Tiruvadi VR, Hwang S-W, Vanleer AC, Wulsin DF, Davis K, Gelber CE, Palmer L, Van der Spiegel J, Wu J, Xiao J, Huang Y, Contreras D, Rogers JA, Litt B, Flexible, foldable, actively multiplexed, high-density electrode array for mapping brain activity in vivo, Nat. Neurosci 14, 1599–605 (2011). [PubMed: 22081157]
22. Khodagholy D, Doublet T, Gurfinkel M, Quilichini P, Ismailova E, Leleux P, Herve T, Sanaur S, Bernard C, Malliaras GG, Highly conformable conducting polymer electrodes for in vivo recordings, Adv. Mater 23, H268–H272 (2011). [PubMed: 21826747]
23. Li J, Wang P, Huang HJ, Dry Epidermal Electrodes Can Provide Long-Term High Fidelity Electromyography for Limited Dynamic Lower Limb Movements, Sensors (Basel). 20, 4848 (2020).

24. Searle A, Kirkup L, A direct comparison of wet, dry and insulating bioelectric recording electrodes, Physiol. Meas 21, 271–283 (2000). [PubMed: 10847194]
25. Jensen GC, Krause CE, Sotzing GA, Rusling JF, Inkjet-printed gold nanoparticle electrochemical arrays on plastic. Application to immunodetection of a cancer biomarker protein, Phys. Chem. Chem. Phys 13, 4888–4894 (2011). [PubMed: 21212889]
26. Mattana G, Loi A, Woytasik M, Barbaro M, Noël V, Piro B, Inkjet-Printing: A New Fabrication Technology for Organic TransistorsAdv. Mater. Technol 2, 1700063 (2017).
27. Lewinski N, Colvin V, Drezek R, Cytotoxicity of nanopartides Small 4, 26–49 (2008). [PubMed: 18165959]
28. Gao M, Li L, Song Y, Inkjet printing wearable electronic devices J. Mater. Chem C 5, 2971–2993 (2017).
29. Kraft U, Molina-Lopez F, Son D, Bao Z, Murmann B, Ink Development and Printing of Conducting Polymers for Intrinsically Stretchable Interconnects and Circuits, Adv. Electron. Mater 6, 1900681 (2020).
30. Sethumadhavan V, Zuber K, Bassell C, Teasdale PR, Evans D, Hydrolysis of doped conducting polymers, Commun. Chem 3, 153 (2020).
31. Park S, An J, Potts JR, Velamakanni A, Murali S, Ruoff RS, Hydrazine-reduction of graphite- and graphene oxide, Carbon N. Y 49, 3019–3023 (2011).
32. Mattevi C, Eda G, Agnoli S, Miller S, Mkhoyan KA, Celik O, Mastrogiovanni D, Granozzi G, Carfunkel E, Chhowalla M, Evolution of electrical, chemical, and structural properties of transparent and conducting chemically derived graphene thin films, Adv. Funct. Mater 19, 2577–2583 (2009).
33. Hantanasirisakul K, Zhao MQ, Urbankowski P, Halim J, Anasori B, Kota S, Ren CE, Barsoum MW, Gogotsi Y, Fabrication of Ti3C2Tx MXene Transparent Thin Films with Tunable Optoelectronic Properties, Adv. Electron. Mater 2, 1600050 (2016).
34. Mariano M, Mashtalir O, Antonio FQ, Ryu WH, Deng B, Xia F, Gogotsi Y, Taylor AD, Solution-processed titanium carbide MXene films examined as highly transparent conductors, Nanoscale 8, 16371–16378 (2016). [PubMed: 27722443]
35. Kim SJ, Choi J, Maleski K, Hantanasirisakul K, Jung HT, Gogotsi Y, Ahn CW, Interfacial assembly of ultrathin, functional MXene films, ACS Appl. Mater. Interfaces 11, 32320–32327 (2019). [PubMed: 31405272]
36. Quain E, Mathis TS, Kurra N, Maleski K, Van Aken KL, Alhabeb M, Alshareef HN, Gogotsi Y, Direct Writing of Additive-Free MXene-in-Water Ink for Electronics and Energy Storage, Adv. Mater. Technol 4, 1800256 (2019).
37. Zhang C, McKeon L, Kremer MP, Park S-H, Ronan O, Seral-Ascaso A, Barwich S, Coileáin CÓ, McEvoy N, Nerl HC, Anasori B, Coleman JN, Gogotsi Y, Nicolosi V, Additive-free MXene inks and direct printing of micro-supercapacitors, Nat. Commun 10, 1795 (2019). [PubMed: 30996224]
38. Dai C, Lin H, Xu G, Liu Z, Wu R, Chen Y, Biocompatible 2D Titanium Carbide(MXenes) Composite Nanosheets for pH-Responsive MRI-Guided Tumor Hyperthermia, Chem. Mater 29, 8637–8652 (2017).
39. Vitale F, Driscoll N, Murphy B, in 2D Metal Carbides and Nitrides (MXenes): Structure, Properties and Applications, Anasori B, Gogotsi Y, Eds. (Springer International Publishing, Cham, 2019), pp. 503–524.
40. Han X, Huang J, Lin H, Wang Z, Li P, Chen Y, 2D Ultrathin MXene-Based Drug-Delivery Nanoplatform for Synergistic Photothermal Ablation and Chemotherapy of Cancer, Adv. Healthc. Mater 7, 1701394 (2018).
41. Meng F, Seredych M, Chen C, Gura V, Mikhalovsky S, Sandeman S, Ingavle G, Ozulumba T, Miao L, Anasori B, Gogotsi Y, MXene Sorbents for Removal of Urea from Dialysate: A Step toward the Wearable Artificial Kidney, ACS Nano 12, 10518–10528 (2018). [PubMed: 30257087]
42. Li L, Fu X, Chen S, Uzun S, Levitt AS, Shuck CE, Han W, Gogotsi Y, Hydrophobic and Stable MXene−Polymer Pressure Sensors for Wearable Electronics, Cite This ACS Appl. Mater. Interfaces 12, 15362–15369 (2020).

43. Seyedin S, Uzun S, Levitt A, Anasori B, Dion G, Gogotsi Y, Razal JM, MXene Composite and Coaxial Fibers with High Stretchability and Conductivity for Wearable Strain Sensing Textiles, Adv. Funct. Mater 30, 1910504 (2020).
44. Driscoll N, Richardson AG, Maleski K, Anasori B, Adewole O, Lelyukh P, Escobedo L, Cullen DK, Lucas TH, Gogotsi Y, Vitale F, Two-Dimensional Ti3C2 MXene for High-Resolution Neural Interfaces, ACS Nano 12, 10419–10429 (2018). [PubMed: 30207690]
45. Driscoll N, Maleski K, Richardson AG, Murphy B, Anasori B, Lucas TH, Gogotsi Y, Vitale F, Fabrication of Ti3C2 MXene microelectrode arrays for in vivo neural recording, J. Vis. Exp 2020, 1–9 (2020).
46. Murphy BB, Mulcahey PJ, Driscoll N, Richardson AG, Robbins GT, V Apollo N, Maleski K, Lucas TH, Gogotsi Y, Dillingham T, Vitale F, A Gel-Free $Ti_3C_2T_x$-Based Electrode Array for High-Density, High-Resolution Surface Electromyography, Adv. Mater. Technol 5, 2000325 (2020). [PubMed: 33693054]
47. Zhang J, Kong N, Uzun S, Levitt A, Seyedin S, Lynch PA, Qin S, Han M, Yang W, Liu J, Wang X, Gogotsi Y, Razal JM, Scalable Manufacturing of Free-Standing, Strong $Ti_3C_2T_x$MXene Films with Outstanding Conductivity, Adv. Mater 32, 2001093 (2020).
48. Mathis T, Maleski K, Goad A, Sarycheva A, Anayee M, Foucher AC, Stach E, Gogotsi Y, Mathis C, Mathis TS, Maleski K, Goad A, Sarycheva A, Anayee M, Alexandre C, Modified MAX Phase Synthesis for Environmentally Stable and Highly Conductive Ti3C2 MXene, ACS Nano 15, 6420–6429 (2021). [PubMed: 33848136]
49. Shuck CE, Sarycheva A, Anayee M, Levitt A, Zhu Y, Uzun S, Balitskiy V, Zahorodna V, Gogotsi O, Gogotsi Y, Scalable Synthesis of $Ti_3C_2T_x$ MXene, Adv. Eng. Mater 22, 1901241 (2020).
50. Alhabeb M, Maleski K, Anasori B, Lelyukh P, Clark L, Sin S, Gogotsi Y, Guidelines for Synthesis and Processing of Two-Dimensional Titanium Carbide (Ti3C2Tx MXene), Chem. Mater 29, 7633–7644 (2017).
51. Uzun S, Seyedin S, Stoltzfus AL, Levitt AS, Alhabeb M, Anayee M, Strobel CJ, Razal JM, Dion G, Gogotsi Y, Knittable and Washable Multifunctional MXene-Coated Cellulose Yarns, Adv. Funct. Mater 29, 1905015 (2019).
52. Franks W, Schenker I, Schmutz P, Hierlemann A, Impedance characterization and modeling of electrodes for biomedical applications, IEEE Trans. Biomed. Eng 52, 1295–1302 (2005). [PubMed: 16041993]
53. Cogan SF, Troyk PR, Ehrlich J, Plante TD, Detlefsen DE, Potential-biased, asymmetric waveforms for charge-injection with activated iridium oxide (AIROF) neural stimulation electrodes, IEEE Trans. Biomed. Eng 53, 327–332 (2006). [PubMed: 16485762]
54. Grill WM, Mortimer JT, Stimulus Waveforms for Selective Neural Stimulation, IEEE Eng. Med. Biol. Mag 14, 375–385 (1995).
55. Cogan SF, Neural stimulation and recording electrodes., Annu. Rev. Biomed. Eng 10, 275–309 (2008). [PubMed: 18429704]
56. Lorencova L, Bertok T, Filip J, Jerigova M, Velic D, Kasak P, Mahmoud KA, Tkac J, Highly stable Ti3C2Tx (MXene)/Pt nanoparticles-modified glassy carbon electrode for H2O2 and small molecules sensing applications, Sensors Actuators, B Chem. 263, 360–368 (2018).
57. Green RA, Toor H, Dodds C, Lovell NH, Variation in performance of platinum electrodes with size and surface roughness, Sensors Mater. 24, 165–180 (2012).
58. Ling Z, Ren CE, Zhao MQ, Yang J, Giammarco JM, Qiu J, Barsoum MW, Gogotsi Y, Flexible and conductive MXene films and nanocomposites with high capacitance, Proc. Natl. Acad. Sci. U. S. A 111, 16676–16681 (2014). [PubMed: 25389310]
59. Zhang CJ, Anasori B, Seral-Ascaso A, Park S-H, McEvoy N, Shmeliov A, Duesberg GS, Coleman JN, Gogotsi Y, Nicolosi V, Transparent, Flexible, and Conductive 2D Titanium Carbide (MXene) Films with High Volumetric Capacitance, Adv. Mater 29, 1702678 (2017).
60. Anasori B, Lukatskaya MR, Gogotsi Y, 2D metal carbides and nitrides (MXenes) for energy storage, Nat. Rev. Mater 2, 16098 (2017).
61. Ganji M, Tanaka A, Gilja V, Halgren E, Dayeh SA, Scaling Effects on the Electrochemical Stimulation Performance of Au, Pt, and PEDOT:PSS Electrocorticography Arrays, Adv. Funct. Mater 27, 1703019 (2017).

62. Hewson DJ, Langeron Y, Duche J, Evolution in impedance at the electrode-skin interface of two types of surface EMG electrodes during long-term recordings, J. Electromyogr. Kinesiol 13, 273–279 (2003). [PubMed: 12706606]
63. Li G, Wang S, Duan YY, Towards gel-free electrodes: A systematic study of electrode-skin impedance, Sensors Actuators, B Chem. 241, 1244–1255 (2017).
64. Lee SM, Byeon HJ, Lee JH, Baek DH, Lee KH, Hong JS, Lee SH, Self-adhesive epidermal carbon nanotube electronics for tether-free long-term continuous recording of biosignals, Sci. Rep 4, 6074 (2014). [PubMed: 25123356]
65. Chen YH, Op de Beeck M, Vanderheyden L, Carrette E, Mihajlović V, Vanstreels K, Grundlehner B, Gadeyne S, Boon P, van Hoof C, Soft, comfortable polymer dry electrodes for high quality ECG and EEG recording, Sensors 14, 23758–23780 (2014). [PubMed: 25513825]
66. Ferree TC, Luu P, Russell GS, Tucker DM, Scalp electrode impedance, infection risk, and EEG data quality, Clin. Neurophysiol 112, 536–544 (2001). [PubMed: 11222977]
67. Klimesch W, EEG alpha and theta oscillations reflect cognitive and memory performance: Are view and analysisBrain Res. Rev 29, 169–195 (1999). [PubMed: 10209231]
68. Li Y, Long J, Yu T, Yu Z, Wang C, Zhang H, Guan C, An EEG-based BCI system for 2-D cursor control by combining Mu/Beta rhythm and P300 potential, IEEE Trans. Biomed. Eng 57, 2495–2505 (2010). [PubMed: 20615806]
69. Hwang H-J, Kwon K, Im C-H, Neurofeedback-based motor imagery training for brain-computer interface (BCI), J. Neurosci. Methods 179, 150–156 (2009). [PubMed: 19428521]
70. Robinson AK, Venkatesh P, Boring MJ, Tarr MJ, Grover P, Behrmann M, Very high-density EEG elucidates spatiotemporal aspects of early visual processing, Sci. Rep 7, 1–11 (2017). [PubMed: 28127051]
71. Wynter S, Dissabandara L, A comprehensive review of motor innervation of the hand: variations and clinical significance, Surg. Radiol. Anat 40, 259–269 (2018). [PubMed: 28725918]
72. Masuda T, Sadoyama T, Distribution of innervation zones in the human biceps brachii, J. Electromyogr. Kinesiol 1, 107–115 (1991). [PubMed: 20870500]
73. Morris TL, Miller JC, Electrooculographic and performance indices of fatigue during simulated flight, Biol. Psychol 42, 343–360 (1996). [PubMed: 8652752]
74. Usakli AB, Gurkan S, Aloise F, Vecchiato G, Babiloni F, On the use of electrooculogram for efficient human computer interfaces, Comput. Intell. Neurosci 2010, 135629 (2010).
75. Berman JI, Berger MS, Mukherjee P, Henry RG, Diffusion-tensor imaging-guided tracking of fibers of the pyramidal tract combined with intraoperative cortical stimulation mapping in patients with gliomas, J. Neurosurg 101, 66–72 (2004). [PubMed: 15255253]
76. Morrell MJ, Responsive cortical stimulation for the treatment of medically intractable partial epilepsy, Neurology 77, 1295–1304 (2011). [PubMed: 21917777]
77. Lee B, Kramer D, Salas MA, Kellis S, Brown D, Dobreva T, Klaes C, Heck C, Liu C, Andersen RA, Engineering artificial somatosensation through cortical stimulation in humans, Front. Syst. Neurosci 12, 24 (2018). [PubMed: 29915532]
78. Schenck JF, The role of magnetic susceptibility in magnetic resonance imaging: MRI magnetic compatibility of the first and second kinds, Med. Phys 23, 815–850 (1996). [PubMed: 8798169]
79. Duyn JH, The future of ultra-high field MRI and fMRI for study of the human brainNeuroimage 62, 1241–1248 (2012). [PubMed: 22063093]
80. Wei H, Bruns OT, Kaul MG, Hansen EC, Barch M, Wiśniowska A, Chen O, Chen Y, Li N, Okada S, Cordero JM, Heine M, Farrar CT, Montana DM, Adam G, Ittrich H, Jasanoff A, Nielsen P, Bawendi MG, Exceedingly small iron oxide nanoparticles as positive MRI contrast agents, Proc. Natl. Acad. Sci. U. S. A 114, 2325–2330 (2017). [PubMed: 28193901]
81. Neumann W, Pusch TP, Siegfarth M, Schad LR, Stallkamp JL, CT and MRI compatibility of flexible 3D-printed materials for soft actuators and robots used in image-guided interventions, Med. Phys 46, 5488–5498 (2019). [PubMed: 31587313]
82. Choi S, Han SI, Jung D, Hwang HJ, Lim C, Bae S, Park OK, Tschabrunn CM, Lee M, Bae SY, Yu JW, Ryu JH, Lee SW, Park K, Kang PM, Lee WB, Nezafat R, Hyeon T, Kim DH, Highly conductive, stretchable and biocompatible Ag–Au core–sheath nanowire composite for wearable and implantable bioelectronics, Nat. Nanotechnol 13, 1048–1056 (2018). [PubMed: 30104619]

83. Bareket L, Inzelberg L, Rand D, David-Pur M, Rabinovich D, Brandes B, Hanein Y, Temporary-tattoo for long-term high fidelity biopotential recordings, Sci. Rep 6, 1–8 (2016). [PubMed: 28442746]
84. Cai K, Haris M, Singh A, Kogan F, Greenberg JH, Hariharan H, Detre JA, Reddy R, Magnetic resonance imaging of glutamate, Nat. Med 18, 302–306 (2012). [PubMed: 22270722]
85. Davis KA, Nanga RPR, Das S, Chen SH, Hadar PN, Pollard JR, Lucas TH, Shinohara RT, Litt B, Hariharan H, Elliott MA, Detre JA, Reddy R, Glutamate imaging (GluCEST) lateralizes epileptic foci in nonlesional temporal lobe epilepsy, Sci. Transl. Med 7, 309ra161 (2015).
86. Cogan SF, Ludwig KA, Welle CG, Takmakov P, Tissue damage thresholds during therapeutic electrical stimulation, J Neural Eng 13, 21001 (2016).
87. Zhao M, Trainor N, Ren CE, Torelli M, Anasori B, Gogotsi Y, Scalable Manufacturing of Large and Flexible Sheets of MXene/Graphene Heterostructures, Adv. Mater. Technol 4, 1800639 (2019).
88. Zhang J, Yang H, Shen G, Cheng P, Zhang J, Guo S, Reduction of graphene oxide via l-ascorbic acid, Chem. Commun 46, 1112–1114 (2010).
89. Barry RJ, Clarke AR, Johnstone SJ, Magee CA, Rushby JA, EEG differences between eyes-closed and eyes-open resting conditions, Clin. Neurophysiol 118, 2765–2773 (2007). [PubMed: 17911042]
90. Jonker ZD, van der Vliet R, Hauwert CM, Gaiser C, Tulen JHM, van der Geest JN, Donchin O, Ribbers GM, Frens MA, Selles RW, TMS motor mapping: Comparing the absolute reliability of digital reconstruction methods to the golden standard, Brain Stimul. 12, 309–313 (2019). [PubMed: 30497885]
91. Ulyanova AV, Koch PF, Cottone C, Grovola MR, Adam CD, Browne KD, Weber MT, Russo RJ, Gagnon KG, Smith DH, Isaac Chen H, Johnson VE, Kacy Cullen D, Wolf JA, Electrophysiological signature reveals laminar structure of the porcine hippocampus, eNeuro 5, e0102–18.2018 (2018).
92. Ganji M, Elthakeb AT, Tanaka A, Gilja V, Halgren E, Dayeh SA, Scaling Effects on the Electrochemical Performance of poly(3,4-ethylenedioxythiophene (PEDOT), Au, and Pt for Electrocorticography Recording, Adv. Funct. Mater 27, 1703018 (2017).
93. Luo X, Weaver CL, Zhou DD, Greenberg R, Cui XT, Highly stable carbon nanotube doped poly(3,4-ethylenedioxythiophene) for chronic neural stimulation, Biomaterials 32, 5551–5557 (2011). [PubMed: 21601278]
94. Lu Y, Lyu H, Richardson AG, Lucas TH, Kuzum D, Flexible Neural Electrode Array Based-on Porous Graphene for Cortical Microstimulation and Sensing, Sci. Rep 6, 33526 (2016). [PubMed: 27642117]
95. Vitale F, Summerson SR, Aazhang B, Kemere C, Pasquali M, Neural Stimulation and Recording with Bidirectional, Soft Carbon Nanotube Fiber Microelectrodes, ACS Nano 9, 4465–4474 (2015). [PubMed: 25803728]
96. Weiland JD, Anderson DJ, Humayun MS, In vitro electrical properties for iridium oxide versus titanium nitride stimulating electrodes, IEEE Trans. Biomed. Eng 49, 1574–1579 (2002). [PubMed: 12549739]
97. Jiang C, Li L, Hao H, Carbon nanotube yarns for deep brain stimulation electrode, IEEE Trans. Neural Syst. Rehabil. Eng 19, 612–616 (2011). [PubMed: 21859605]

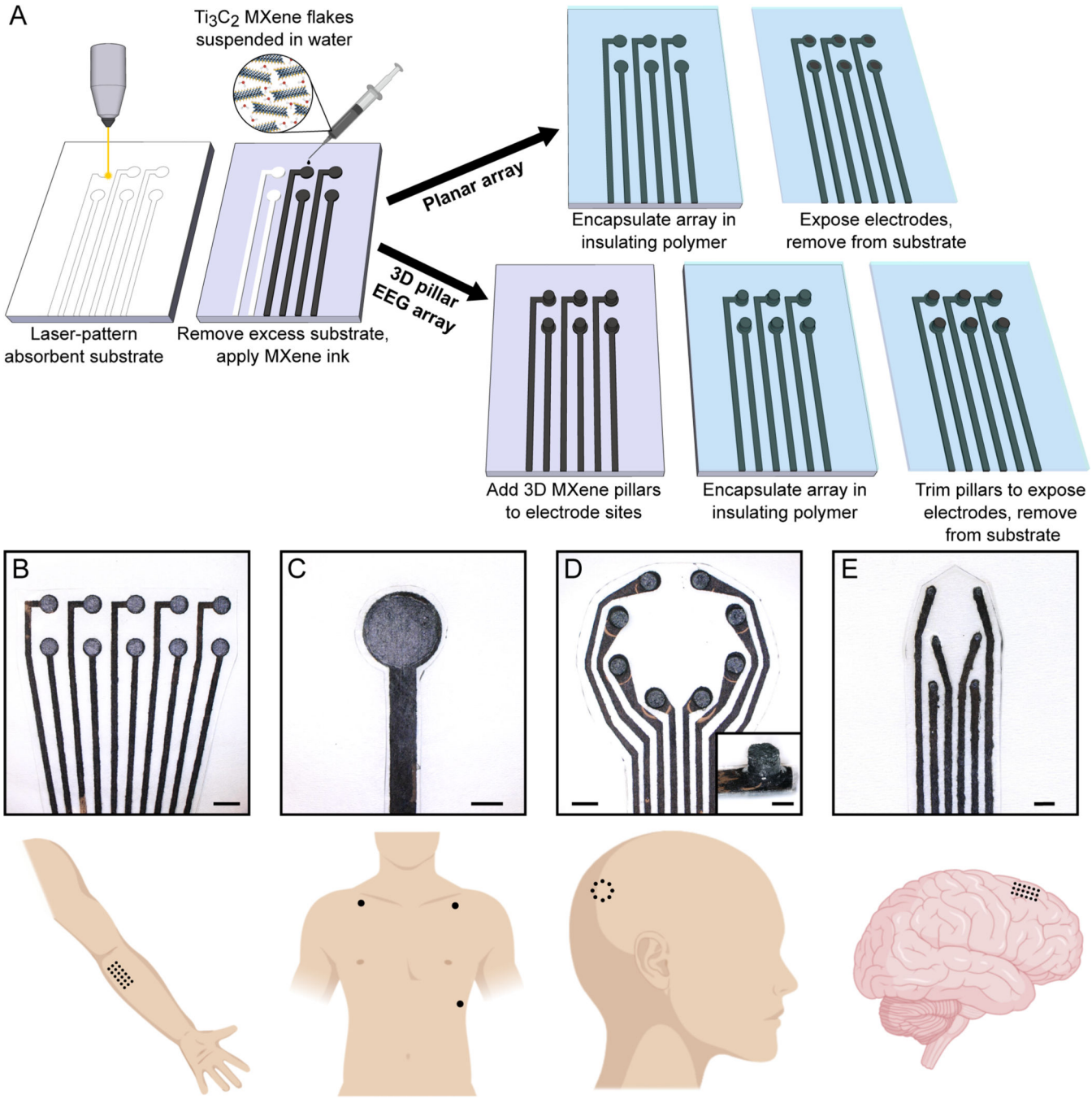


**Fig. 1. Rapid, high-throughput manufacturing of MXtrodes, MXene ink-infused bioelectronics.**

(**A**) Schematic of the fabrication method for laser-patterned planar and 3D mini-pillar MXene electrode arrays. (**B** to **E**) Photographs of different electrode array geometries (top) and schematics of their intended anatomic application sites (bottom): (B) EMG, (C) ECG, (D) EEG, and (E) ECoG monitoring. Scale bars: (B to D) 5 mm; inset in (D) and (E) 2 mm.

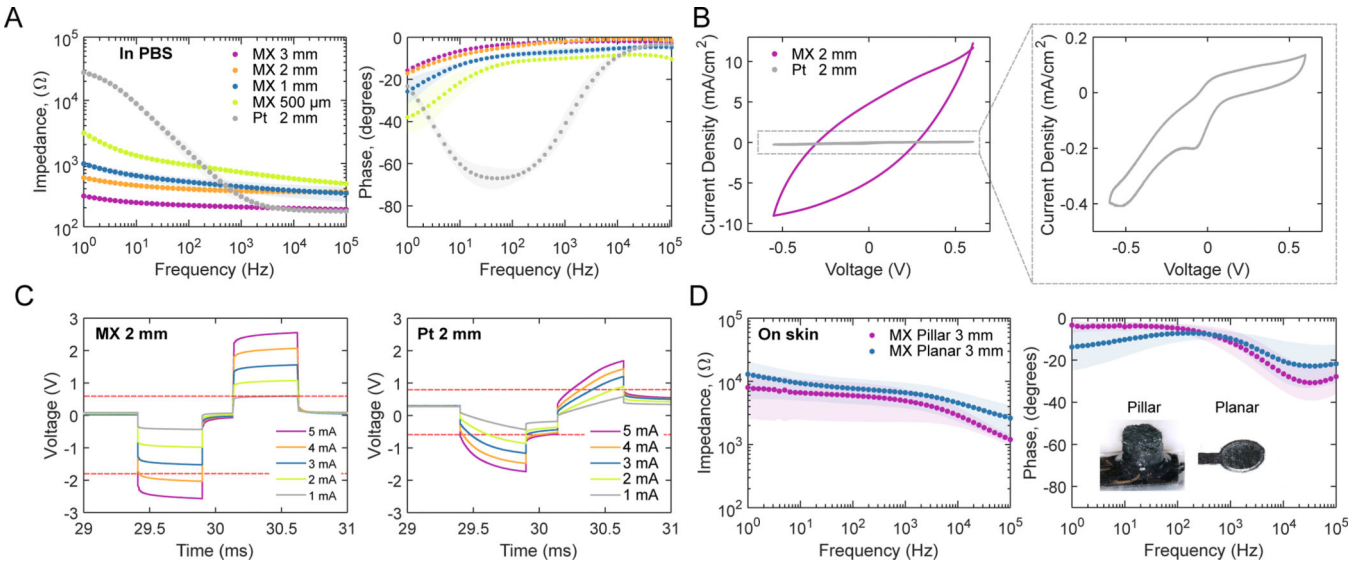


**Fig. 2. Electrochemical properties of MXtrodes.**

(**A**) EIS spectra measured in 1X PBS for 3 mm, 2 mm, 1 mm, and 500 µm planar MXene electrodes compared to 2 mm Pt electrodes (n=10 per type). Data are plotted as means with shaded regions corresponding to SDs. (**B**) CVs for representative 2 mm planar MXtrode and Pt electrodes scanned from −0.6 to +0.6 V at 50 mV/s. (**C**) Voltage transients in response to biphasic current pulses, with $t_c = t_a = 500$ µs and $t_{ip} = 250$ µs, current amplitudes ranging from 1 to 5 mA for representative 2 mm planar MXtrode and Pt electrodes. Anodic and cathodic voltage limits for MXene and Pt are displayed on their respective plots as dashed red lines. (**D**) EIS spectra measured on skin for 3 mm MXtrode 3D pillar and planar electrodes (n=10 per type). Data are plotted as means with shaded regions corresponding to SDs.

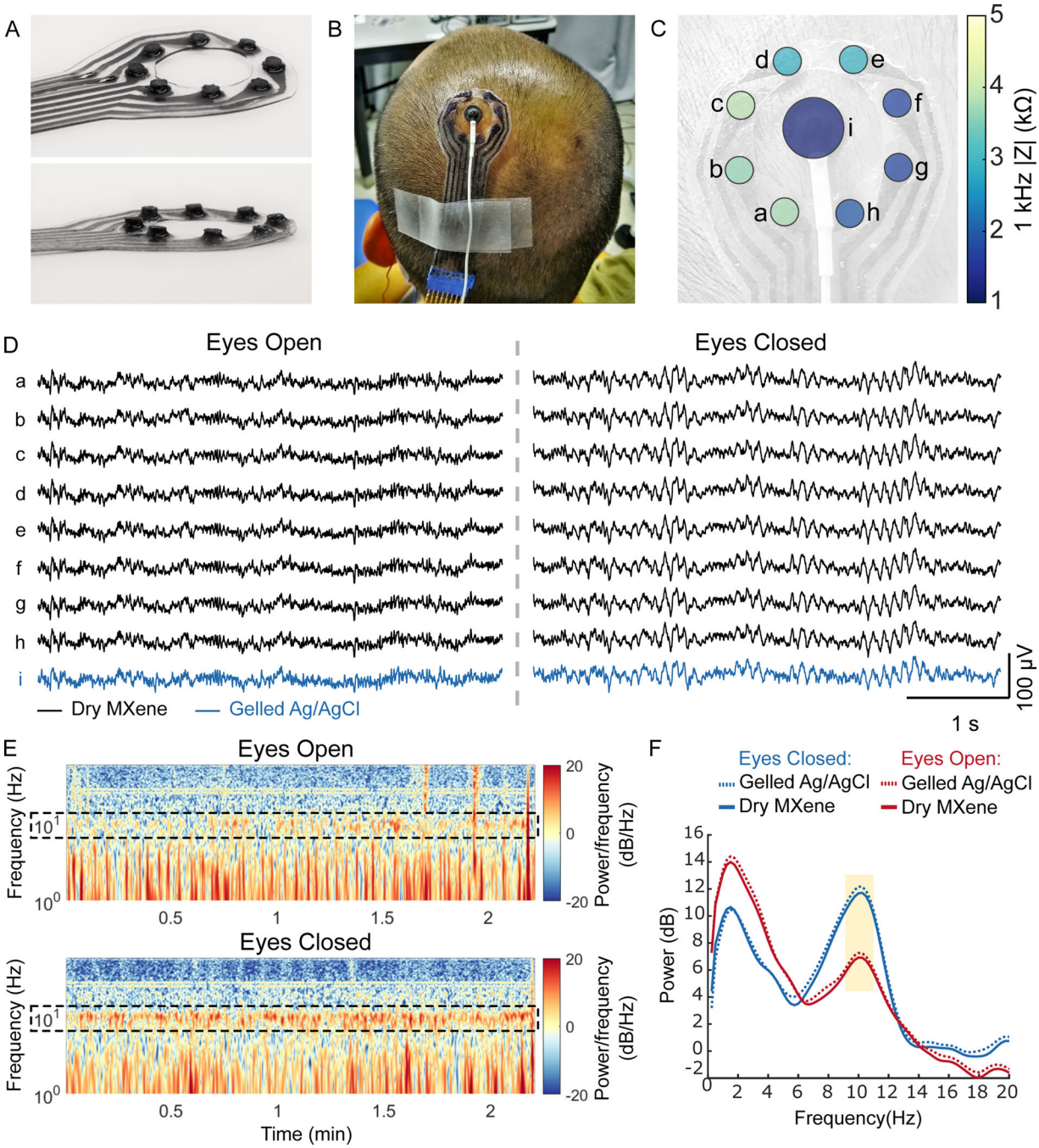


**Fig. 3. Dry EEG recording enabled by 3D pillar MXtrodes.**

(**A**) Photographs of a MXtrode 3D EEG array with eight 3 mm-diameter MXene electrodes in a circular arrangement around a central opening. (**B**) Photograph of MXtrode electrode array and standard gelled Ag/AgCl cup electrode placed on head of human subject. (**C**) Map of 1 kHz impedance values for all electrodes on the subject's head. (**D**) Segments of recorded EEG signal from all electrodes during the eyes open (left) and eyes closed (right) tasks at resting state on one subject. (**E**) Spectrograms of the EEG signal recorded on MXene electrode b in the eyes open (top) and eyes closed (bottom) conditions. Alpha

frequency band is enclosed in dashed box to highlight differences between eyes open and eyes closed states, which were consistent across 4 recording epochs. (**F**) Power spectral density during eyes open and eyes closed EEG recordings. The 8–12 Hz alpha band is highlighted.

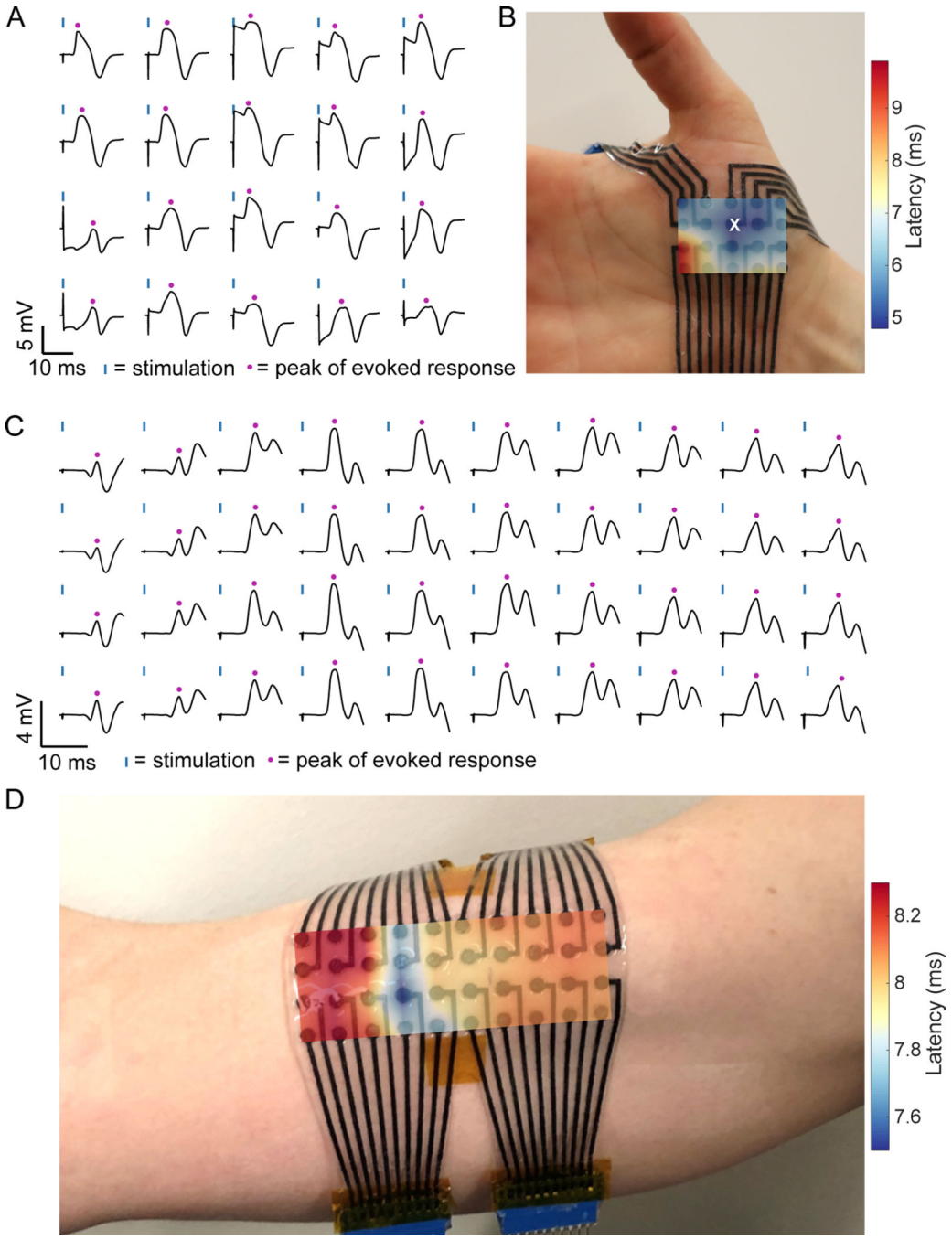


**Fig. 4. High density surface EMG mapping with MXtrode arrays.**

(**A** and **B**) EMG recordings from the APB muscle. (A) Average evoked response following N=10 median nerve stimulation epochs recorded on 20-ch MXtrode array placed over APB. Blue ticks indicate time of nerve stimulation, and purple dots indicate time of peak evoked response. (B) Latency map of peak response overlaid on photo of the MXtrode array on the APB. White “x” indicates the channel with shortest latency, corresponding to the IZ. (**C** and **D**) EMG recordings from the biceps muscle. (C) Average evoked response following N=10 supraclavicular nerve stimulation epochs recorded on 40-ch MXtrode array placed over the

biceps. Blue ticks indicate time of nerve stimulation, and purple dots indicate time of peak evoked response. (D) Latency map of peak response overlaid on photo of the MXtrode array on the subject's biceps. Distributed IZ running perpendicular to the muscle is apparent as the band with the shortest latency. Data collected from N=1 subject for each muscle group.

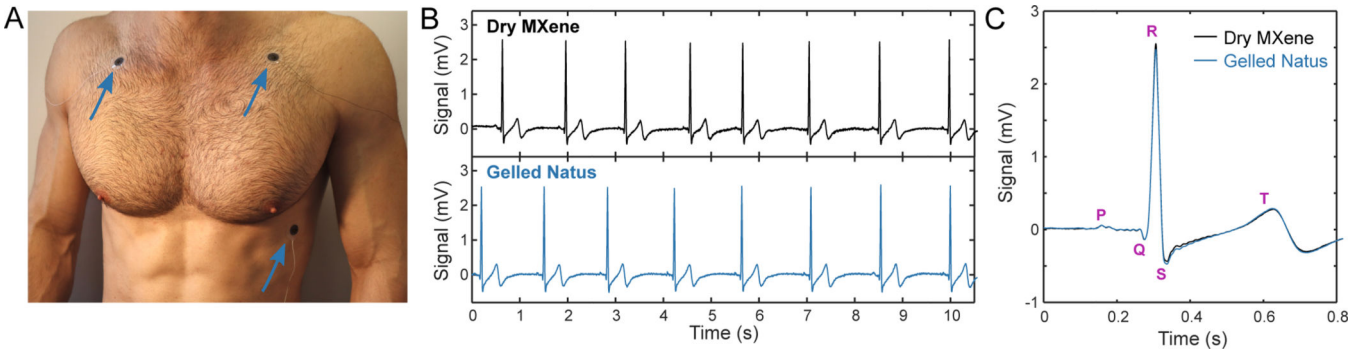


**Fig. 5. Electrocardiography with MXtrodes.**

(**A**) Photograph of ECG recording setup. Electrodes were interchanged in the same locations (blue arrows) to obtain sequential recordings from either dry MXene or pre-gelled commercial electrodes. (**B**) Ten seconds of ECG recordings on the dry MXtrodes (top) and the pre-gelled commercial electrodes (bottom). (**C**) Average ECG waveforms recorded on the two electrode types, marked with salient ECG features. Data collected from N=1 subject.

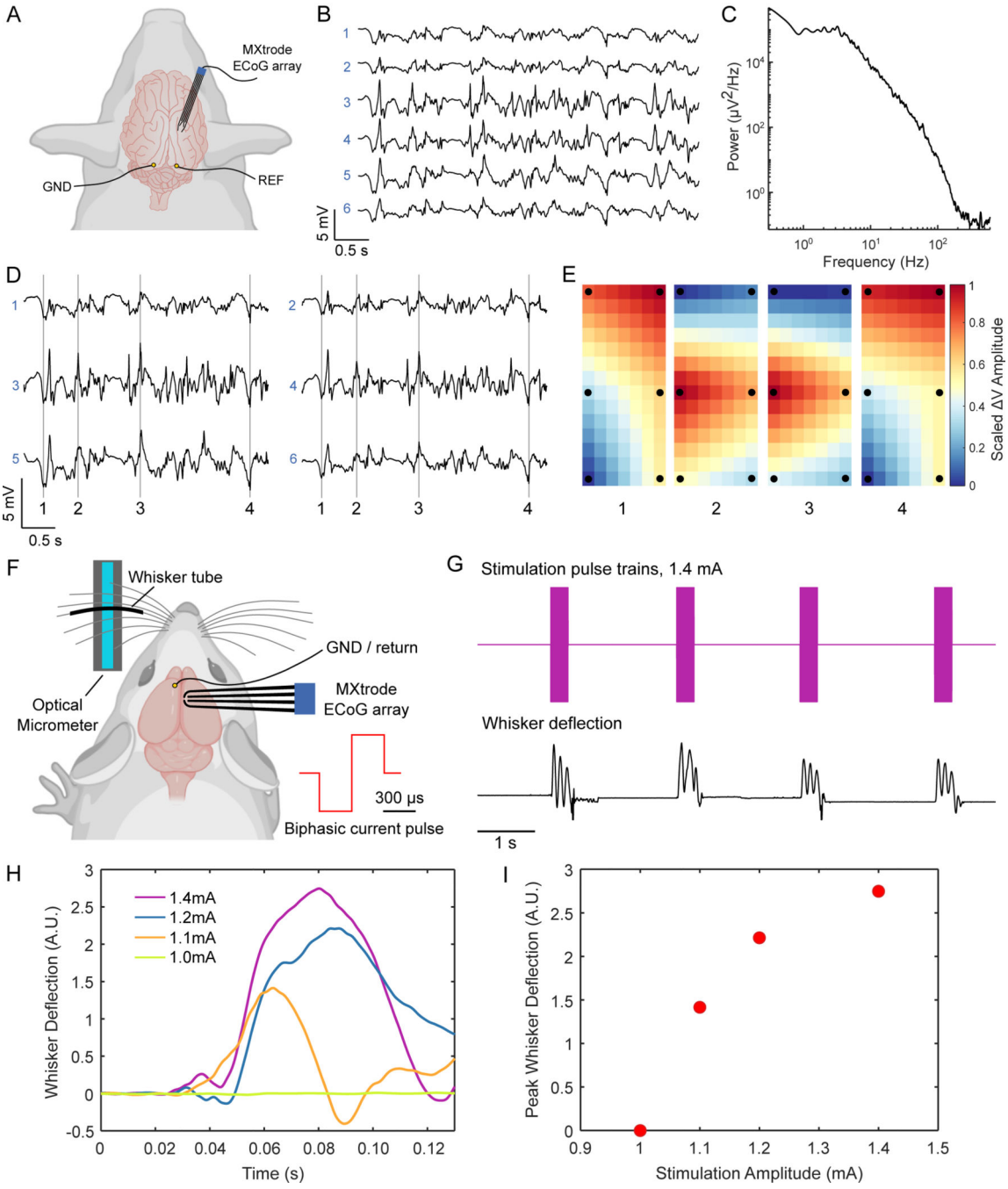


**Fig. 6. ECoG recording and cortical stimulation with MXtrode arrays.**

(**A**) Schematic depicting ECoG recording setup with the 6-ch array of 500 μm-diameter MXtrodes placed subdurally on somatosensory cortex of N=1 pig. (**B**) A few seconds of representative ECoG data recorded on the MXtrode array. (**C**) Power spectral density of the ECoG recording. (**D**) Segment of ECoG data, displayed according to the spatial arrangement of the 6 MXtrodes. (**E**) Instantaneous voltage mapping recorded across the 6 MXtrodes during down states (panels 1 and 4) and up states (panels 2 and 3). The timing of these voltage maps is indicated in (D) by the vertical lines. Voltage was interpolated across

the array and normalized, with black dots indicating location of the 6 MXtrode contacts. (**F**) Schematic of the cortical stimulation setup, with the 4-ch array of 500 μm-diameter MXtrodes placed over barrel cortex, and the optical micrometer used to detect and amplify the whisker deflection signal in N=1 rat. (**G**) Whisker deflection data recorded by the optical micrometer during a series of stimulation pulse trains delivered at 1.4 mA. (**H**) Average first whisker deflection for each stimulation pulse amplitude, time-aligned by the stimulation onset (n=10 stimulation trails per current amplitude). (**I**) Scaling of whisker deflection amplitude with stimulation amplitude.

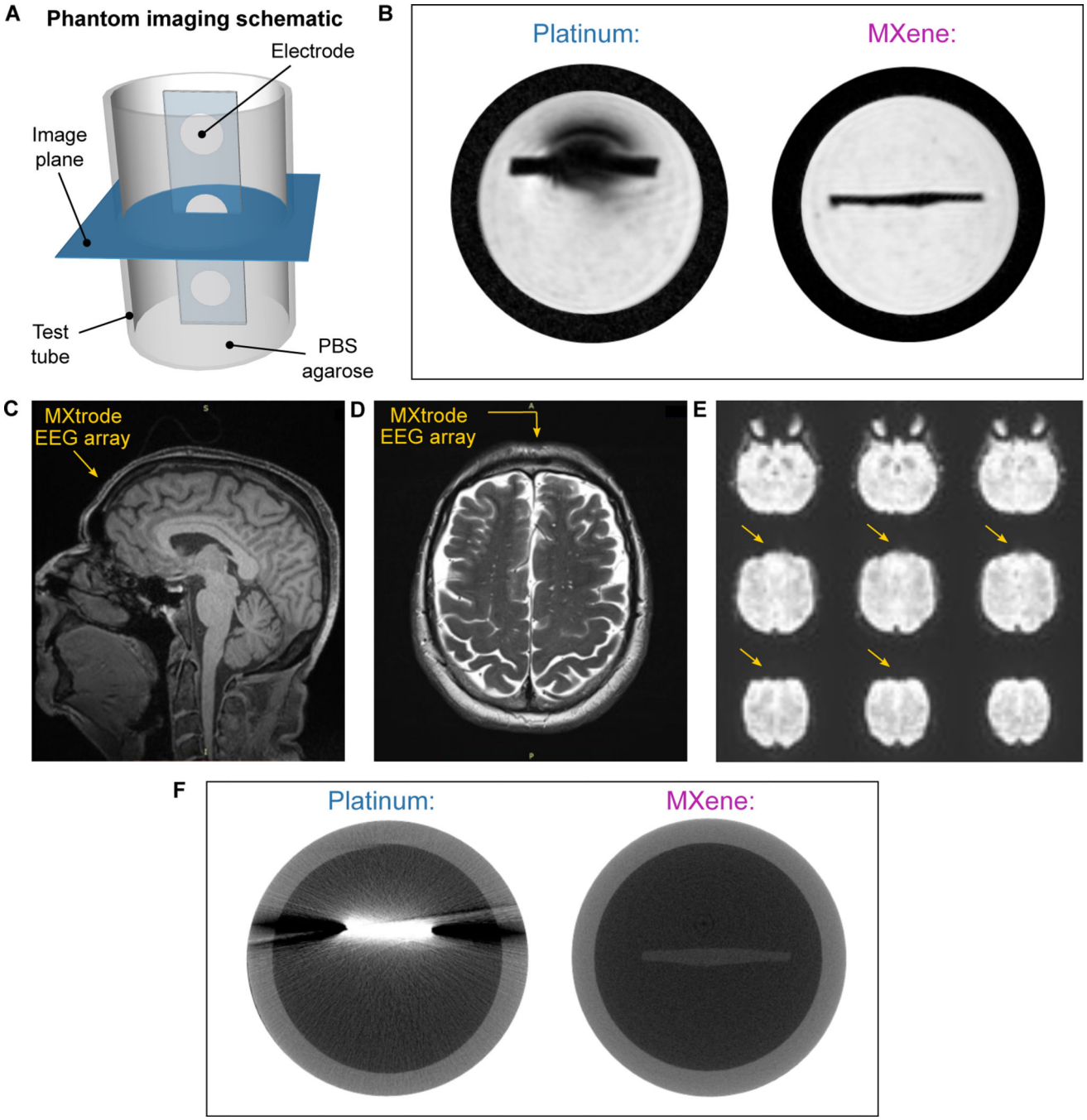


**Fig. 7. MRI and CT compatibility of MXtrodes.**

(**A**) Schematic of the phantom imaging setup used for 9.4T MRI and CT imaging. Strips of disk electrodes (3 mm-diameter MXtrodes or 2.3 mm-diameter clinical Pt ECoG strip electrodes) were embedded in a conductive agarose phantom and imaged in the transverse plane. (**B**) High-field 9.4T MRI scans for Pt electrode (left) and MXtrode (right). (**C-E**) MXtrode EEG array placed on human forehead and imaged in 3T clinical scanner using (**C**) T1 weighted MPRAGE, (**D**) T2 weighted FLAIR, (**E**) HCP resting BOLD fMRI scan

sequences. Location of MXtrode array on the subject's forehead is indicated by the arrows. (**F**) High-resolution CT scans for Pt electrode (left) and MXtrode (right).

**Table 1.**

**Summary of electrochemical properties of planar MXtrodes of varying diameters, compared to a 2 mm-diameter Pt electrode contact.**

For each type of electrode, N=10 for |Z| values and N=5 for $CSC_C$ and $CIC_C$ values.

| Material | Electrode diameter | 1 kHz \|Z\| in PBS (Ω) | 10 Hz \|Z\| in PBS (Ω) | Potential Limits vs. Ag/AgCl (V) | $CSC_C$ (mC $cm^{-2}$) | $CIC_C$ (mC $cm^{-2}$) |
|---|---|---|---|---|---|---|
| MXene | 3 mm | 205.6 ± 11.1 | 241.4 ± 14.7 | −1.7 –0.6 | 157.9 ± 19.6 | 0.53 ± 0.08 |
| | 2 mm | 369.2 ± 40.2 | 451.2 ± 35.4 | −1.7 –0.6 | 306.3 ± 35.2 | 0.67 ± 0.03 |
| | 1 mm | 430.2 ± 86.1 | 644.2 ± 97.3 | −1.7 –0.6 | 607.8 ± 90.2 | 1.02 ± 0.07 |
| | 500 μm | 729.2 ± 71.2 | 1343.3 ± 81.6 | −1.7 –0.6 | 1495.3 ± 60.5 | 2.01 ± 0.46 |
| Pt | 2 mm | 301.7 ± 77.6 | 8918.3 ± 1147.7 | −0.6 –0.8 | 4.4 ± 0.7 | 0.05 ± 0.001 |